ACS SENSORS

pubs.acs.org/acssensors

Letter

Converging Multidimensional Sensor and Machine Learning Toward High-Throughput and Biorecognition Element-Free Multidetermination of Extracellular Vesicle Biomarkers

Caroline Y. N. Nicoliche,[#] Ricardo A. G. de Oliveira,[#] Giulia S. da Silva,[#] Larissa F. Ferreira, Ian L. Rodrigues, Ronaldo C. Faria, Adalberto Fazzio, Emanuel Carrilho, Letícia G. de Pontes, Gabriel R. Schleder, and Renato S. Lima*

Cite This: *ACS Sens.* 2020, 5, 1864−1871

Read Online

ACCESS | Metrics & More | Article Recommendations | Supporting Information

ABSTRACT: Extracellular vesicles (EVs) are a frontier class of circulating biomarkers for the diagnosis and prognosis of different diseases. These lipid structures afford various biomarkers such as the concentrations of the EVs (C_V) themselves and carried proteins (C_P). However, simple, high-throughput, and accurate determination of these targets remains a key challenge. Herein, we address the simultaneous monitoring of C_V and C_P from a single impedance spectrum without using recognizing elements by combining a multidimensional sensor and machine learning models. This multidetermination is essential for diagnostic accuracy because of the heterogeneous composition of EVs and their molecular cargoes both within the tumor itself and among patients. Pencil HB cores acting as electric double-layer capacitors were integrated into a scalable microfluidic device, whereas supervised models provided accurate predictions, even from a small number of training samples. User-friendly measurements were performed with sample-to-answer data processing on a smartphone. This new platform further showed the highest throughput when compared with the techniques described in the literature to quantify EVs biomarkers. Our results shed light on a method with the ability to determine multiple EVs biomarkers in a simple and fast way, providing a promising platform to translate biofluid-based diagnostics into clinical workflows.

KEYWORDS: *point-of-care diagnosis, accuracy, smartphone, exosome, cancer*

Extracellular vesicles (EVs) consist of lipid nanoparticles (50 to 200 nm in diameter) released by cells into the circulation and have emerged as a promising class of biomarkers for the diagnosis and prognosis of diseases such as cancer and Alzheimer's disease.[1,2] These structures remain stable over weeks, are abundant in biofluids, and carry molecular cargoes such as proteins, nucleic acids, and lipids, which are either inherited from parent cells or exist as membrane-bound molecules.[3] Accordingly, the circulating EVs reflect the molecular status of their parent cells and further afford multiple biomarkers, e.g., the amounts of EVs themselves and proteins (cell-inherited and extravesicular).[4−6]

Despite the clinical potential of EVs and their contents, accurate and high-throughput monitoring of these targets remains an important challenge. Conventional techniques for EVs analysis (Western blotting, ELISA, flow cytometry, and counting methods) usually have poor sensibility, need a large quantity of samples (>500 μL), and demand laborious purification procedures prior to analysis. New sensors have been developed to monitor EVs biomarkers, which are generally based on sandwich immunoassays or EVs magnetic isolation. While these approaches are promising, they typically require time-consuming (>1 h) tests.[1,3]

A further sensing challenge facing the monitoring of EVs biomarkers is the high heterogeneity in their biomolecular composition both within the tumor itself and among patients.[3] In this regard, the analysis of multiple biomarkers is key to ensure accurate diagnoses.[7] To circumvent this limitation, the simultaneous quantification of EVs and carried extravesicular proteins is addressed herein for the first time by converging a multidimensional sensor and machine learning tasks toward rapid, sample-to-answer, and accurate multideterminations as demonstrated in Scheme 1. After EVs isolation (10 min) using a low-cost technique (<$9.00 per sample) based on size exclusion chromatography, mice blood samples were analyzed by an impedimetric microfluidic chip (<6 min) bearing ready-to-use and cross-reactive probes. Concentrations of both EVs (C_V) and extravesicular proteins (C_P) could be meaured from a single impedance spectrum with the aid of supervised models,

Received: March 25, 2020
Accepted: June 29, 2020
Published: June 29, 2020

Scheme 1. Illustration of the Strategy to Quantify EVs Biomarkers[a]

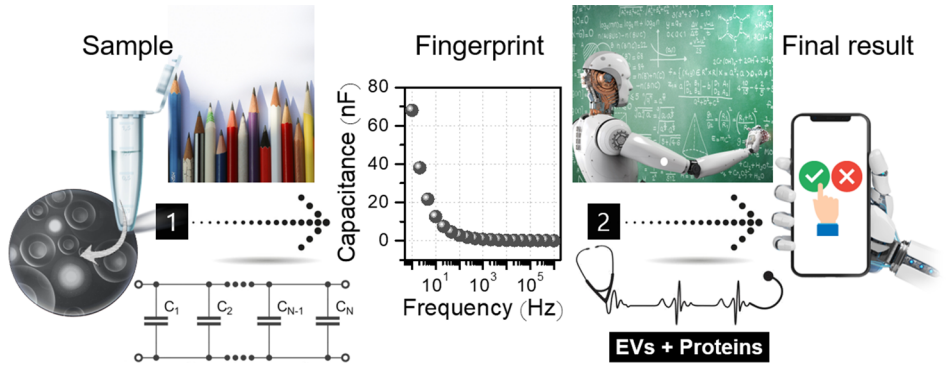

[a]Samples extracted from mice blood with isolated EVs are tested by the sensor bearing pencil core-based probes, which acted as parallel capacitors (1). The amounts of EVs and proteins could be shown on a smartphone by treating the capacitances through machine learning models (2). Adapted with permission from Shutterstock. Copyrights [2017, 2019].

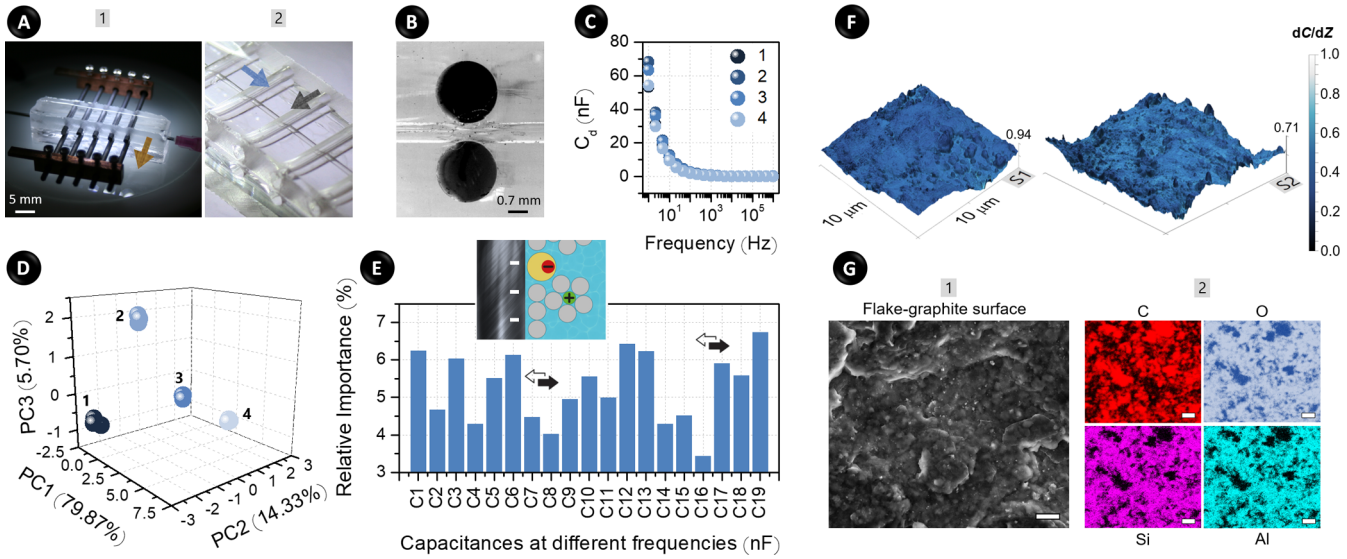

Figure 1. Device, differential readout, and electrodes. (A) PDMS microfluidic chip. (B) Stereoscopic image of the sample channel in contact with cross sections of two electrode channels (in black) that are related to one EDL capacitor. (C) Plots of C_d vs frequency for KCl 4.0 mol L^{-1} reached after renewing (1−4) the HB cores (n = 3) and (D) resulting PCA scores plots. (E) Relative importance of the C_d features for discriminatory by RF model. (F) dC/dZ merged on 3D R_{RMS} images of two core areas (S1,S2). (G) SEM image (1) and color maps of C, O, Si, and Al on the same area (2). In (A), the yellow arrow indicates the sliding direction for renewing the electrodes (1), whereas the blue and gray arrows highlight the sample and electrode channels, respectively (2). C_d is diversified in three regions as indicated by arrows in (E) and discussed in the main text. The specification of the capacitances (C1 to C19) in (E) is shown in the Supporting Information. Its inset shows the EDL with anion specific adsorption. In (G), the scale bars on the SEM image and color maps correspond to 1 and 25 μm, respectively.

without using separation or targeting elements (e.g., antibodies or aptamers).

Multidimensional sensors have emerged as a potential alternative for multitarget analysis.[8] These sensing arrays respond to a class of species (global selectivity) with different sensibilities (cross-sensibility), thus creating fingerprint-like responses that are treated by statistical learning models for the recognition of samples.[9,10] Conventional sensing arrays demand the combination of specific receptors with distinct cross-reactive probes and the use of a large number of training samples to afford accurate multidetermination models.[11−13] Otherwise, we herein show the sample-to-answer, high-throughput, simultaneous, and accurate monitoring of EVs biomarkers, even from a small training subset. Broadly available scholar pencil graphite was employed as a cross-reactive and ready-to-use single probe.

Graphite cores (HB scale) were reversibly incorporated into low-cost and scalable microfluidic chips of polydimethylsiloxane (PDMS) and operated as an association of five electric double-layer (EDL) capacitors in parallel as exhibited in Figures 1A and S1. In contrast to traditional arrays that involve the fabrication of different probes and succeeding assays,[14] the fingerprints were herein achieved from a single scan of differential capacitance (C_d)[15] vs frequency due to chemical diversification of the equivalent C_d data as it has been developed by our group.[16−19]

Microfluidic devices composed of the PDMS elastomer were fabricated by a bondless, scalable, and cleanroom-free method that is based on sequential steps of polymerization and scaffold removal as highlighted in the Supporting Information.[20−22] The sample channel had a diameter of 700.0 μm. The HB cores were reversibly inserted above and below the sample channel as exhibited in Figure 1B, avoiding laborious routines

https://dx.doi.org/10.1021/acssensors.0c00599
ACS Sens. 2020, 5, 1864−1871

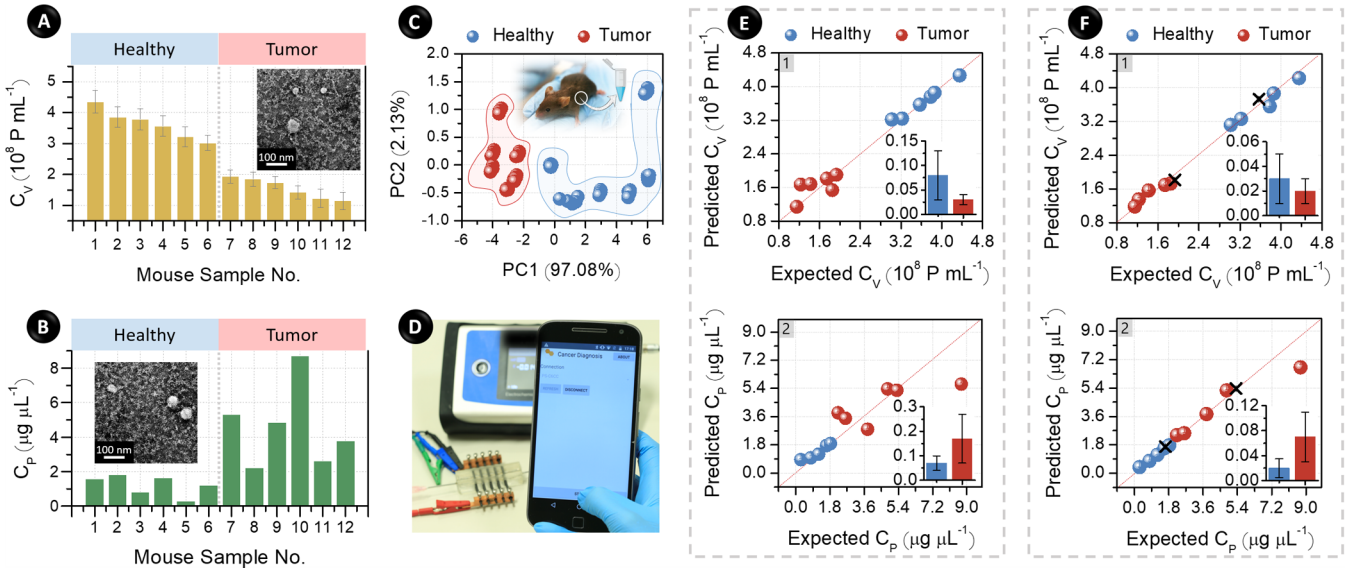

Figure 2. Analysis of EVs. True data of (A) C_V by NTA and (B) C_P by Bradford assay. (C) PCA scores plots by our chip to treated mice samples as indicated. Adapted with permission from Shutterstock. Copyright [2013]. (D) Our setup with the sensor, potentiostat, and smartphone. Fittings of predicted vs expected C_V (1) and C_P (2) from (E) SISSO and (F) RF. Insets in (A,B) show TEM images of tumor and healthy EVs, respectively. In (A), the error bars mean confidence intervals for $\alpha = 0.05$ ($n = 3$, 1498 frames). These intervals were lower than 0.2 $\mu g\ \mu L^{-1}$ ($n = 3$) in (B). In (E,F), the red dashed lines correspond to the ideal behavior. Their insets show average confidence intervals (10^8 P mL^{-1} in 1 and $\mu g\ \mu L^{-1}$ in 2) to EVs from healthy (blue) and tumor (red) mice ($n = 8$).

to irreversibly attach electrodes to the device.[22] Five pairs of pencil cores were short-circuited with copper pieces to achieve an association of five polarizable capacitors in parallel.

Spectra of C_d vs dc potential and frequency show high chemical diversification, thus increasing cross-sensibility with a consequent improvement on recognition ability of the sensor. The potential-based capacitances depend on the differential ion and dipole arrangements on EDL around the potential of zero charge (PZC). In terms of the frequency-based plots, these capacitance data are diversified into three regions.[18] Ions in solution are able to follow the excitation electric field oscillations at low frequencies and then charge the electrode/liquid interface forming the EDL capacitance that mainly drives C_d at values lower than 10^2 Hz. The electrode material is the driving effect at intermediate frequencies. At high frequencies (>10^5 Hz), the ions are not capable of migrating toward interfaces and C_d is then dominated by the geometric capacitance with sample (bulk) working as the dielectric medium.[23,24]

Chemical diversification of the C_d data was also provided by the HB cores as revealed by measurements of KCl 4.0 mol L^{-1}. In practice, different electrode surfaces were exposed to the solution by renewing the cores after recording C_d vs potential and frequency ($n = 3$). Such renewal was based on manually sliding the probes across the sample channel (Figure 1A). The capacitances were calculated from imaginary impedances and angular frequencies assuming the sensing probes as ideally polarizable electrodes (see the Supporting Information).[25,26]

From spectra and principal component analysis (PCA) plots in Figure 1C,D, respectively, the data of C_d vs frequency by the four renewed HB core areas were distinct from each other. Similar behavior was attained for the data of C_d vs potential (Figure S2). These data show a heterogeneous EDL capacitive charging along the core surfaces, thus indicating that different C_d outputs are obtained even from the core pairs in contact with the sample in the same assay. Such diversified data lead to an enhanced recognition ability since the equivalent C_d achieved by the sensor comprises contributions of the individual capacitors.[16−19] In comparison with the potential-based data, the plots as a function of frequency provided the best classification performance (data not shown) and then were considered in the following analyses.

Using supervised random forests (RF) model (tree depth of 25 and 500 estimators), the relative importance of the features for data classification could be calculated as exhibited in Figure 1E. Capacitances at the three previously mentioned regions of frequency presented high relevance. The precision of the analyses was satisfactory, with the confidence intervals ($\alpha = 0.05$) ranging from 41.6 pF (for C_d up to 10^1 Hz) to 4.3 nF (for the other C_d data).

The spectra of C_d vs potential (Figure S2) presented different values of PZC to each electrode renewal. These PZCs were negative (−0.31 to −0.38 V), thus confirming the incidence of anions specifically adsorbed on graphite (inset of Figure 1E).[15,27] These adsorptions are crucial for sensing performance by increasing the dispersion of C_d with frequency.[25] These deviations in PZC, along with the discrepancies in C_d vs frequency, are likely owing to heterogeneous chemical composition and surface area of the HB cores (see the Supporting Information), as it was indeed confirmed by energy-dispersive X-ray spectroscopy (EDS) and atomic force microscopy (AFM), respectively.

While capacitance gradient (dC/dZ) values by AFM electrical analyses revealed only a small heterogeneity as shown in Figures 1F and S3, the root-mean-square roughness (R_{RMS}) showed high a discrepancy in five core areas of 10 μm × 10 μm. Their values were 121.3 ± 23.8, 79.0 ± 24.5, 142.2 ± 13.5, 137.8 ± 23.8, and 110.6 ± 27.2 nm ($n = 4$), whereas the global R_{RMS} was calculated as 118.2 ± 15.7 ($n = 16$). One should note that such high roughness data favor the occurrence of specific adsorptions at EDL,[25] thus increasing the cross-sensibility of the sensing array.

https://dx.doi.org/10.1021/acssensors.0c00599
ACS Sens. 2020, 5, 1864−1871

From 2D SEM image (100 μm^2) in Figure 1G, the HB core is composed of flake-graphite, the most common natural graphite. The relative amounts of C, O, Si, and Al on probe surfaces were heterogeneous (Figure S4, Table S1) as well. In four regions of size (250.000 μm^2) similar to the detection areas into the device, Si and Al ranged from ∼8% to ∼15%. The color maps of O, Si, and Al had the same 2D profile (Figure 1G) in accordance with their covalently bonded incidence on clay minerals.

In addition to the C═C/C—C peaks associated with graphite, results by X-ray photoelectron spectroscopy (XPS) revealed the occurrence of C—O/C═O peaks that are related to fatty alcohols and acids present in wax, respectively (Figure S4). Such groups maximize intermolecular attractions (e.g., electrostatic interactions and hydrogen bonding) with the targets, which are critical for the recognition performance of sensing arrays. The presence of C sp2 is also essential by generating $\pi-\pi$ stacking with amino acids and proteins in bioassays.[28]

The sensor was applied to a total of 12 samples of mice blood with (6) and without (6) Ehrlich tumor that is a neoplasm from female mice breast carcinoma and presents primary features of mammary tumor cells.[29] For EVs isolation, blood samples were treated by size exclusion chromatography using a fast and cheap protocol. The latter is further reported to be reproducible and produce intact EVs purer than ultracentrifugation and precipitation methods.[30,31] Following, EVs and cargoes were diluted in phosphate-buffered saline (PBS) medium for ensuing analyses.

Transmission electron microscopy (TEM) images of typical EVs from tumor and healthy mice are displayed in Figure 2A,B, respectively. From the data of nanoparticle tracking analysis (NTA; Figure S5), the tumor EVs (106 to 700 nm) showed polydispersity larger than the healthy ones (156 to 348 nm). The EVs were mainly composed of lipid structures with roughly 150 nm in diameter that corresponds to exosomes, generated by the repeated inward budding of the endosomal membrane.[3] The values of C_V by NTA in Figure 2A were lower for the diseased EVs ($4.4-1.2 \times 10^8$ particles per mL, P mL^{-1}). The opposite behavior was noted for C_P by Bradford assay ($0.3-8.7$ μg μL^{-1}) as shown in Figure 2B. In this case, the healthy EVs had the lower C_P data.

Using 15 data features at frequencies from 10^1 to 10^6 Hz (see the Supporting Information, Figure S6), the sensor provided the recognition of the healthy and tumor samples as exhibited in the PCA scores plots of Figures 2C and S7 (n = 8). Thus, our sensing strategy may be used for a screening diagnosis. Next, advanced machine learning models were applied to ensure accurate breast cancer stage monitoring from the determination of both C_V and C_P. These tasks relied on a randomized splitting (ratios of 83/17 and 75/25 for splitting the training/testing and training/validation sets, respectively) and 5-fold cross-validation.

First, the C_d data were processed by the supervised sure independence screening and sparsifying operator (SISSO). Recently reported in the literature,[32] SISSO operates by means of simple mathematical equations that compress the original features and provide accurate predictions even from a small training subset, avoiding the need for a large number of samples. Originally proposed to evaluate material properties,[33] SISSO regression models were herein fitted to obtain C_V and C_P assuming the data by NTA and Bradford assay methods as the true contents (expected data). The final SISSO equations reduced the original 15 C_d features to 6 (C_V) and 5 data (C_P) as shown below

$$C_V = a_1|(C9/C5) - (C13/C9)| + a_2|(C8/C3) - (C13/C6)| + b_1 \quad (1)$$

$$C_P = a_3|(C8/C1) - (C15/C9)| + a_4|(C9/C2) - (C14/C6)| + b_2 \quad (2)$$

wherein the constants a and b are defined in the Supporting Information.

Only capacitances at frequencies lower than 10^5 Hz were selected by SISSO, indicating the EVs were able to migrate to the electrode/liquid interfaces, contributing to EDL charging. PBS-diluted EVs are negatively charged phospholipid-bilayer membranous structures, showing zeta potentials of around −20 mV.[34] Only a few features at low frequencies (<10^2 Hz, C1 to C4) were picked. This result is supposed to be tightly tied to the electrode polarization effects, in which the charging by free ions common to all samples (present in PBS in our case) mainly drives the EDL capacitance.[35] While the solution resistance is basically governed by the buffer,[15] the cell geometry (gap and area of the cores) was constant over all the analyses since the probes were not renewed in this case. These parameters modify the geometric capacitance that is, thereby, expected to remain invariable as noted herein (Figure S6). This phenomenon supports the absence of high-frequency C_d in the previous modeled SISSO equations.

The adjusted SISSO models endowed the chip with the ability to attain C_V and C_P in a simple way by considering the device prototyping, sample preparation, detection, and data processing. The latter routine is usually laborious, especially when machine learning methods are used, hindering the development of effective point-of-care tests.[36] Taking up the potential use of sample-to-answer analytical techniques for user-friendly experiments, an Android app was further written with Xamarin (open-source app platform) to automatically quantify the values of C_V and C_P on smartphone from SISSO as exhibited in Figure 2D. The app was able to control a portable potentiostat, acquire C_d, and complete the SISSO tasks. C_V and C_P, along with resulting clinical status (healthy or diseased), were exhibited on the smartphone display without the need for data treatment by the user (Video S1).

The resulting plots of predicted vs true concentrations by the SISSO algorithm are shown in Figure 2E. These data indicate a linear trend for both the EVs biomarkers, with a better overall predictive ability for C_V than for C_P. In the first case, the linear fitting had intersection close to 0 and slope near 1, with R^2 and mean absolute error (MAE) of 0.94 and 0.2×10^8 P mL^{-1}, respectively. While a poorer predictive capability (R^2 < 0.68 and MAE < 1.0 μg μL^{-1}) was achieved in the second situation, a satisfactory accuracy was noted for the healthy samples.

By once again using the biomarker contents from NTA and Bradford assay as the true data, a multioutput regression based on a single RF model (tree depth of 13 and 239 estimators) was also employed to improve the multidetermination accuracy as it was indeed verified herein. In this case, the fingerprints consisted of C_d features throughout the frequency spectra and resulted in a satisfactory correlation as shown in Figure 2F. In fact, the accuracies were close to the ideal

https://dx.doi.org/10.1021/acssensors.0c00599
ACS Sens. 2020, 5, 1864−1871

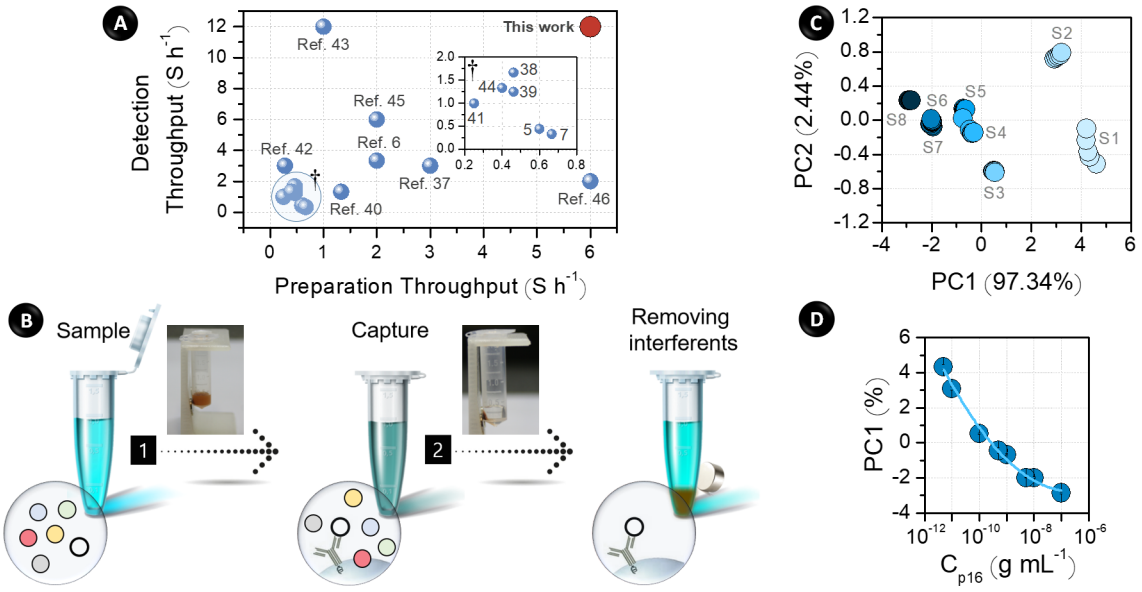

Figure 3. Comparison with literature and protein selective analysis. (A) Ability of methods addressed in the literature to treat (e.g., from blood to serum) and sensing samples per h (S h^{-1}) to monitor EVs biomarkers. (B) Main steps to capture p16. Adapted with permission from Shutterstock. Copyright [2017]. (C) PCA scores plots and (D) analytical curve for standards of p16. In (A), the references are underlined and its inset highlights the marked region (†). In (B), photos of the sample after adding MBs-Ab (1) and during magnetic separation (2) are shown. The p16/antibody binding is exhibited in the bottom inset of (2). In (C), S1−S8 mean the increasing analytical concentrations of p16 (C_{p16}) as highlighted in the analytical curve of (D).

behavior for both C_V ($R^2 > 0.99$ and MAE < 0.1×10^8 P mL^{-1}) and C_P ($R^2 > 0.92$ and MAE < 0.7 $\mu g\ \mu L^{-1}$) (Figure S8).

Assuming 2.4×10^8 P mL^{-1} and 2.2 $\mu g\ \mu L^{-1}$ as the thresholds to define the clinical condition in agreement with NTA (C_V) and Bradford assay (C_P) data, respectively, both the learning models of SISSO and RF led to successful discrimination of the healthy and diseased sample groups. However, since these models rely on randomized iterations, several final analytical solutions were obtained depending on the selected testing subset because of the small number of training samples. Nonetheless, the same trend was obtained in all the cases, with similar prediction abilities. Such results show the robustness of the models. One should also emphasize the low dispersion of the data points indicates once again a satisfactory precision.

The sensor further exhibited a high lifetime, which is crucial for its daily applicability by minimizing the impacts of its poor reproducibility that arises from the heterogeneous surface of the HB cores (see Figure 1D). In practice, 60 samples of lake spiked with multiple heavy metals were analyzed by two operators on different days (Figure S9, Table S2). Machine learning tasks assured accurate classification and multi-determination tasks with reproducibility.

Considering both steps of sample preparation and detection, to our knowledge, this new platform presents the highest throughput when compared with the approaches reported in the literature to quantify EVs cargoes as shown in Figure 3A. Such sensors are typically based on sandwich-type immunoassays or EVs magnetic isolation.[5−7,37−46] To guarantee accurate analyses, these methods may require additional assays on each sample to correct variations in the EVs concentration among patients.[6] Therefore, in addition to enhancing the diagnostic accuracy, the detection of both EVs and proteins as described herein is advantageous for sensor simplicity and analytical frequency.

By means of magnetic isolation and enrichment by resuspension in water as usually described in the literature for EVs analysis, our sensor was also successfully used in the specific quantification of p16, a peptide whose expression is correlated to the incidence and stage of prostate and cervical tumors.[47] Our chip could directly detect the target in dispersion as exhibited in Figure 3B, dispensing the usage of active labels on secondary antibodies as commonly needed. Briefly, the analytical routine was based on magnetic beads modified with p16 antibody (MB-Ab) for p16 immunocapture. Following, the peptide was isolated by applying an external magnetic field and, then enriched by resuspending the formed MB-Ab-p16 conjugates in water. Afterwards, this aqueous dispersion was inserted into the device for impedimetric measurements.

The responses comprised six features, i.e., C_d at five frequencies (2.2, 4.6, 10.0, 21.5, and 46.4 Hz) and PZC. By treating the data by PCA, p16 standards were well-distinguished as shown in the scores plots of Figure 3C. Since PC2 was lower than 3%, only PC1 was collected to acquire the analytical curve as shown in Figure 3D. Nonlinear fitting ($R^2 > 0.99$) resulted in a limit-of-detection of 0.6 pg mL^{-1} that is lower than the values addressed in the literature.[47−49] While experiments on real samples are still necessary to assess its effective potential, these preliminary data show the sensor may be attractive for specific analyses as well.

Further study will evaluate a greater number of samples originating from patients with different pathologies to scrutinize the effective sensor lifetime and model robust learning algorithms that can be used not only to predict C_V and C_P but also to monitor other EVs cargos. The latter ability further advances the potential use of the device to diagnose and guide the treatment of numerous diseases. Future investigation will also exploit different sensing arrays that can be classified into three classes, i.e., disposable sensors such as the microfluidic paper-based analytical chips, high-performance

https://dx.doi.org/10.1021/acssensors.0c00599
ACS Sens. 2020, 5, 1864−1871

sensors fabricated by conventional photolithography-based processes, and long-lifetime sensors.

In summary, our results demonstrated that this new method is capable of classifying healthy and tumor mice samples and quantifying C_V and C_P from single spectra of impedance in a user-friendly, high-throughput, and accurate fashion. While the platforms addressed in the literature require time-consuming experiments and active probes for indirect EVs monitoring, we herein describe that the convergence of a universal sensing array with machine learning tasks and sample-to-answer data treatment on smartphones provides a potential method to assess multiple EVs biomarkers. Combined with a fast EVs isolation method as used herein, this platform may be of paramount relevance to advance and translate clinical diagnostics and therapeutics from research to routine applications. Indeed, our sensing approach meets the most guidelines (sensitive, affordable, user-friendly, delivered, and rapid) of the World Health Organization (WHO) for point-of-care bioanalyses.[36]

Remarkably, the rapid sample preparation method of size exclusion chromatography for EVs isolation and resuspension in saline buffer avoids the drawbacks (sensibility, reproducibility, and accuracy loss) associated with electrode fouling at complex body fluids such as blood, plasma, and serum.[50] Such an advantage contributes to the manufacturing of simpler electrode designs. One should also highlight that the developed strategy may be attractive for mass individual testing by eliminating the use of recognizing species. Mass testing is crucial for taking pandemic combat actions and restoring civil liberties as we have been witnessing nowadays with the COVID-19 pandemic.[51] The requirement for antibodies and other bioreagents has hindered the global supply of fast diagnosis kits, especially in low-income countries.

■ ASSOCIATED CONTENT

Supporting Information

The Supporting Information is available free of charge at https://pubs.acs.org/doi/10.1021/acssensors.0c00599.

Chemicals and samples, prototyping of the chip, electrode characterization, EVs isolation, monitoring, and characterization, data treatment, differential potential-based readout, data to heavy metal-spiked lake samples, and specific determination of biomarker (PDF)

Analysis process using smartphone to control a portable potentiostat, acquire the capacitance data, and make the machine learning tasks (MP4)

■ AUTHOR INFORMATION

Corresponding Author

Renato S. Lima − *Brazilian Nanotechnology National Laboratory, Brazilian Center for Research in Energy and Materials, Campinas, São Paulo 13083-970, Brazil; Institute of Chemistry, University of Campinas, Campinas, São Paulo 13083-970, Brazil;* orcid.org/0000-0001-8450-1475; Email: renato.lima@lnnano.cnpem.br

Authors

Caroline Y. N. Nicoliche − *Brazilian Nanotechnology National Laboratory, Brazilian Center for Research in Energy and Materials, Campinas, São Paulo 13083-970, Brazil; Institute of Chemistry, University of Campinas, Campinas, São Paulo 13083-970, Brazil*

Ricardo A. G. de Oliveira − *Brazilian Nanotechnology National Laboratory, Brazilian Center for Research in Energy and Materials, Campinas, São Paulo 13083-970, Brazil*

Giulia S. da Silva − *Brazilian Nanotechnology National Laboratory, Brazilian Center for Research in Energy and Materials, Campinas, São Paulo 13083-970, Brazil; Institute of Chemistry, University of Campinas, Campinas, São Paulo 13083-970, Brazil*

Larissa F. Ferreira − *Brazilian Nanotechnology National Laboratory, Brazilian Center for Research in Energy and Materials, Campinas, São Paulo 13083-970, Brazil; Institute of Chemistry, University of Campinas, Campinas, São Paulo 13083-970, Brazil*

Ian L. Rodrigues − *Brazilian Nanotechnology National Laboratory, Brazilian Center for Research in Energy and Materials, Campinas, São Paulo 13083-970, Brazil*

Ronaldo C. Faria − *Department of Chemistry, Federal University of São Carlos, São Carlos, São Paulo 13565-905, Brazil;* orcid.org/0000-0003-1094-9597

Adalberto Fazzio − *Brazilian Nanotechnology National Laboratory, Brazilian Center for Research in Energy and Materials, Campinas, São Paulo 13083-970, Brazil; Federal University of ABC, Santo André, São Paulo 09210-580, Brazil;* orcid.org/0000-0001-5384-7676

Emanuel Carrilho − *São Carlos Institute of Chemistry, University of São Paulo, São Carlos, São Paulo 13566-590, Brazil;* orcid.org/0000-0001-7351-8220

Letícia G. de Pontes − *São Carlos Institute of Chemistry, University of São Paulo, São Carlos, São Paulo 13566-590, Brazil*

Gabriel R. Schleder − *Brazilian Nanotechnology National Laboratory, Brazilian Center for Research in Energy and Materials, Campinas, São Paulo 13083-970, Brazil; Federal University of ABC, Santo André, São Paulo 09210-580, Brazil;* orcid.org/0000-0003-3129-8682

Complete contact information is available at: https://pubs.acs.org/10.1021/acssensors.0c00599

Author Contributions

#C.Y.N.N., R.A.G.O., and G.S.S. contributed equally to this work.

Notes

The authors declare no competing financial interest.

■ ACKNOWLEDGMENTS

Financial support for this project was provided by The São Paulo Research Foundation (Grants 2018/24214-3, 17/18139-6, and 17/02317-2), Petrobras (Grant 2015/00301-6), and National Institute of Science and Technology in Bioanalytics (Grant 2014/50867-3). Dr. Carlos A. R. Costa, Dr. Jefferson Bettini, and Fabiano E. Montoro are thanked for the support with microscopy images. In addition, we would like to thank Dr. Antonio C. M. Padilha, Dr. Fabiana Marques, Prof. Dr. Valtencir Zucolotto, and Rafael Defavari for helping us with machine learning tasks, mouse sample processing, NTA measurements, and photos, respectively.

■ REFERENCES

(1) Im, H.; Lee, K.; Weissleder, R.; Lee, H.; Castro, C. M. Novel nanosensing technologies for exosome detection and profiling. *Lab Chip* **2017**, *17*, 2892−2898.

(2) Linxweiler, J.; Junker, K. Extracellular vesicles in urological malignancies: an update. *Nat. Rev. Urol.* **2020**, *17*, 11−27.
(3) Lim, C. Z. J.; Zhang, L.; Zhang, Y.; Sundah, N. R.; Shao, H. New Sensors for Extracellular Vesicles: Insights on Constituent and Associated Biomarkers. *ACS Sens* **2020**, *5*, 4−12.
(4) Im, H.; Shao, H.; Park, Y. I.; Peterson, V. M.; Castro, C. M.; Weissleder, R.; Lee, H. Label-free detection and molecular profiling of exosomes with a nano-plasmonic sensor. *Nat. Biotechnol.* **2014**, *32*, 490−495.
(5) Shao, H.; Chung, J.; Lee, K.; Balaj, L.; Min, C.; Carter, B. S.; Hochberg, F. H.; Breakefield, X. O.; Lee, H.; Weissleder, R. Chip-based analysis of exosomal mRNA mediating drug resistance in glioblastoma. *Nat. Commun.* **2015**, *6*, 6999.
(6) Jeong, S.; Park, J.; Pathania, D.; Castro, C. M.; Weissleder, R.; Lee, H. Integrated Magneto-Electrochemical Sensor for Exosome Analysis. *ACS Nano* **2016**, *10*, 1802−1809.
(7) Ko, J.; Bhagwat, N.; Yee, S. S.; Ortiz, N.; Sahmoud, A.; Black, T.; Aiello, N. M.; McKenzie, L.; O'Hara, M.; Redlinger, C.; Romeo, J.; Carpenter, E. L.; Stanger, B. Z.; Issadore, D. Combining Machine Learning and Nanofluidic Technology To Diagnose Pancreatic Cancer Using Exosomes. *ACS Nano* **2017**, *11*, 11182−11193.
(8) Peveler, W. J.; Yazdani, M.; Rotello, V. M. Selectivity and Specificity: Pros and Cons in Sensing. *ACS Sens* **2016**, *1*, 1282−1285.
(9) Wasilewski, T.; Migoń, D.; Gębicki, J.; Kamysz, W. Critical review of electronic nose and tongue instruments prospects in pharmaceutical analysis. *Anal. Chim. Acta* **2019**, *1077*, 14−29.
(10) Braunger, M. L.; Fier, I.; Rodrigues, V.; Arratia, P. E.; Riul, A., Jr. Microfluidic Mixer with Automated Electrode Switching for Sensing Applications. *Chemosensors* **2020**, *8*, 13.
(11) Gutiérrez, M.; Alegret, S.; del Valle, M. Potentiometric bioelectronic tongue for the analysis of urea and alkaline ions in clinical samples. *Biosens. Bioelectron.* **2007**, *22*, 2171−2178.
(12) Mimendia, A.; Legin, A.; Merkoçi, A.; del Valle, M. Use of Sequential Injection Analysis to construct a potentiometric electronic tongue: Application to the multidetermination of heavy metals. *Sens. Actuators, B* **2010**, *146*, 420−426.
(13) Herrera-Chacon, A.; González-Calabuig, A.; Campos, I.; del Valle, M. Bioelectronic tongue using MIP sensors for the resolution of volatile phenolic compounds. *Sens. Actuators, B* **2018**, *258*, 665−671.
(14) Yu, Y.; Joshi, P. C.; Wu, J.; Hu, A. Laser-Induced Carbon-Based Smart Flexible Sensor Array for Multiflavors Detection. *ACS Appl. Mater. Interfaces* **2018**, *10*, 34005−34012.
(15) Bard, A. L.; Faulkner, L. R. *Electrochemical Methods: Fundamentals and Applications*, 2nd ed.; John Wiley & Sons: New York, 2001; pp 368−534.
(16) Shimizu, F. M.; Todao, F. R.; Gobbi, A. L.; Oliveira, O. N., Jr.; Garcia, C. D.; Lima, R. S. Functionalization-Free Microfluidic Electronic Tongue Based on a Single Response. *ACS Sens* **2017**, *2*, 1027−1034.
(17) Shimizu, F. M.; Pasqualeti, A. M.; Todão, F. R.; de Oliveira, J. F. A.; Vieira, L. C. S.; Gonçalves, S. P. C.; da Silva, G. H.; Cardoso, M. B.; Gobbi, A. L.; Martinez, D. S. T.; Oliveira, O. N., Jr.; Lima, R. S. Monitoring the Surface Chemistry of Functionalized Nanomaterials with a Microfluidic Electronic Tongue. *ACS Sens* **2018**, *3*, 716−726.
(18) Nicoliche, C. Y. N.; Costa, G. F.; Gobbi, A. L.; Shimizu, F. M.; Lima, R. S. Pencil graphite core for pattern recognition applications. *Chem. Commun.* **2019**, *55*, 4623−4626.
(19) da Silva, G. S.; de Oliveira, L. P.; Costa, G. F.; Giordano, G. F.; Nicoliche, C. Y. N.; da Silva, A. A.; Khan, L. U.; da Silva, G. H.; Gobbi, A. L.; Silveira, J. V.; Filho, A. G. S.; Schleder, G. R.; Fazzio, A.; Martinez, D. S. T.; Lima, R. S. Ordinary microfluidic electrodes combined with bulk nanoprobe produce multidimensional electric double-layer capacitances towards metal ion recognition. *Sens. Actuators, B* **2020**, *305*, 127482−127493.
(20) de Camargo, C. L.; Shiroma, L. S.; Giordano, G. F.; Gobbi, A. L.; Vieira, L. C. S.; Lima, R. S. Turbulence in microfluidics: cleanroom-free, fast, solventless, and bondless fabrication and application in high throughput liquid-liquid extraction. *Anal. Chim. Acta* **2016**, *940*, 73−83.
(21) Teixeira, C. A.; Giordano, G. F.; Beltrame, M. B.; Vieira, L. C. S.; Gobbi, A. L.; Lima, R. S. Renewable solid electrodes in microfluidics: recovering the electrochemical activity without treating the surface. *Anal. Chem.* **2016**, *88*, 11199−11206.
(22) de Oliveira, R. A. G.; Nicoliche, C. Y. N.; Pasqualeti, A. M.; Shimizu, F. M.; Ribeiro, I. R.; Melendez, M. E.; Carvalho, A. L.; Gobbi, A. L.; Faria, R. C.; Lima, R. S. Low-Cost and Rapid-Production Microfluidic Electrochemical Double-Layer Capacitors for Fast and Sensitive Breast Cancer Diagnosis. *Anal. Chem.* **2018**, *90*, 12377−12384.
(23) de Oliveira, R. F.; Merces, L.; Vello, T. P.; Bufon, C. B. F. Water-gated phthalocyanine transistors: Operation and transduction of the peptideeenzyme interaction. *Org. Electron.* **2016**, *31*, 217−226.
(24) Riul, A., Jr.; Malmegrim, R. R.; Fonseca, F. J.; Mattoso, L. H. C. An artificial taste sensor based on conducting polymers. *Biosens. Bioelectron.* **2003**, *18*, 1365−1369.
(25) Lockett, V.; Sedev, R.; Ralston, J.; Horne, M.; Rodopoulos, T. Differential Capacitance of the Electrical Double Layer in Imidazolium-Based Ionic Liquids: Influence of Potential, Cation Size, and Temperature. *J. Phys. Chem. C* **2008**, *112*, 7486−7495.
(26) Ji, H.; Zhao, X.; Qiao, Z.; Jung, J.; Zhu, Y.; Lu, Y.; Zang, L. L.; MacDonald, A. H.; Ruoff, R. S. Capacitance of carbon-based electrical double-layer capacitors. *Nat. Commun.* **2014**, *5*, 3317.
(27) Bockris, J. O'M.; Reddy, A. K. N.; Gamboa-Aldeco, M. *Modern Electrochemistry: Fundamentals of Electrodics 2A*, Vol. *2*; Kluwer Academic Publishers: New York, 2002; pp 806−919.
(28) Tao, Y.; Ran, X.; Ren, J.; Qu, X. Array-Based Sensing of Proteins and Bacteria By Using Multiple Luminescent Nanodots as Fluorescent Probes. *Small* **2014**, *10*, 3667−3671.
(29) Mishra, S.; Tamta, A. K.; Sarikhani, M.; Desingu, P. A.; Kizkekra, S. M.; Pandit, A. S.; Kumar, S.; Khan, D.; Raghavan, S. C.; Sundaresan, N. R. Subcutaneous Ehrlich Ascites Carcinoma mice model for studying cancer-induced cardiomyopathy. *Sci. Rep.* **2018**, *8*, 5599.
(30) Böing, A. N.; van der Pol, E.; Grootemaat, A. E.; Coumans, F. A. W.; Sturk, A.; Nieuwland, R. Single-step isolation of extracellular vesicles by size-exclusion chromatography. *J. Extracell. Vesicles* **2014**, *3*, 23430.
(31) Lobb, R. J.; Becker, M.; Wen, S. W.; Wong, C. S.; Wiegmans, A. P.; Leimgruber, A.; Möller, A. Optimized exosome isolation protocol for cell culture supernatant and human plasma. *J. Extracell. Vesicles* **2015**, *4*, 27031.
(32) Ouyang, R.; Curtarolo, S.; Ahmetcik, E.; Scheffler, M.; Ghiringhelli, L. M. SISSO: A compressed-sensing method for identifying the best low-dimensional descriptor in an immensity of offered candidates. *Phys. Rev. Materials* **2018**, *2*, 083802.
(33) Schleder, G. R.; Padilha, A. C. M.; Acosta, C. M.; Costa, M.; Fazzio, A. From DFT to machine learning: recent approaches to materials science−a review. *J. Phys. Mater.* **2019**, *2*, 032001.
(34) Stremersch, S.; Brans, T.; Braeckmans, K.; De Smedt, S.; Raemdonck, K. Nucleic acid loading and fluorescent labeling of isolated extracellular vesicles requires adequate purification. *Int. J. Pharm.* **2018**, *548*, 783−792.
(35) Ghobaei Namhil, Z.; Kemp, C.; Verrelli, E.; Iles, A.; Pamme, N.; Adawi, A. M.; Kemp, N. T. A label-free aptamer-based nanogap capacitive biosensor with greatly diminished electrode polarization effects. *Phys. Chem. Chem. Phys.* **2019**, *21*, 681−691.
(36) Yamada, K.; Shibata, H.; Suzuki, K.; Citterio, D. Toward practical application of paper-based microfluidics for medical diagnostics: state-of-the-art and challenges. *Lab Chip* **2017**, *17*, 1206−1249.
(37) Zhao, Z.; Yang, Y.; Zeng, Y.; He, M. A. A microfluidic ExoSearch chip for multiplexed exosome detection towards blood-based ovarian cancer diagnosis. *Lab Chip* **2016**, *16*, 489−496.
(38) Lee, K.; Fraser, K.; Ghaddar, B.; Yang, K.; Kim, E.; Balaj, L.; Chiocca, E. A.; Breakefield, X. O.; Lee, H.; Weissleder, R. Multiplexed Profiling of Single Extracellular Vesicles. *ACS Nano* **2018**, *12*, 494−503.

https://dx.doi.org/10.1021/acssensors.0c00599
ACS Sens. 2020, 5, 1864−1871

(39) Liu, C.; Xu, X.; Li, B.; Situ, B.; Pan, W.; Hu, Y.; An, T.; Yao, S.; Zheng, L. Single-Exosome-Counting Immunoassays for Cancer Diagnostics. *Nano Lett.* **2018**, *18*, 4226−4232.
(40) Zong, S.; Wang, L.; Chen, C.; Lu, J.; Zhu, D.; Zhang, Y.; Wang, Z.; Cui, Y. Facile detection of tumor-derived exosomes using magnetic nanobeads and SERS nanoprobes. *Anal. Methods* **2016**, *8*, 5001−5008.
(41) Liang, K.; Liu, F.; Fan, J.; Sun, D.; Liu, C.; Lyon, C. J.; Bernard, D. W.; Li, Y.; Yokoi, K.; Katz, M. H. Nanoplasmonic Quantification of Tumor-derived Extracellular Vesicles in Plasma Microsamples for Diagnosis and Treatment Monitoring. *Nat. Biomed. Eng.* **2017**, *1*, 0021.
(42) Jiang, Y.; Shi, M.; Liu, Y.; Wan, S.; Cui, C.; Zhang, L.; Tan, W. Aptamer/AuNP Biosensor for Colorimetric Profiling of Exosomal Proteins. *Angew. Chem., Int. Ed.* **2017**, *56*, 11916−11920.
(43) Tavallaie, R.; McCarroll, J.; Le Grand, M.; Ariotti, N.; Schuhmann, W.; Bakker, E.; Tilley, R. D.; Hibbert, D. B.; Kavallaris, M.; Gooding, J. J. Nucleic acid hybridization on an electrically reconfigurable network of gold-coated magnetic nanoparticles enables microRNA detection in blood. *Nat. Nanotechnol.* **2018**, *13*, 1066−1071.
(44) Mathew, D. G.; Beekman, P.; Lemay, S. G.; Zuilhof, H.; Le Gac, S.; van der Wiel, W. G. Electrochemical Detection of Tumor-Derived Extracellular Vesicles on Nanointerdigitated Electrodes. *Nano Lett.* **2020**, *20*, 820−828.
(45) Lim, C. Z. J.; Zhang, Y.; Chen, Y.; Zhao, H.; Stephenson, M. C.; Ho, N. R. Y.; Chen, Y.; Chung, J.; Reilhac, A.; Loh, T. P.; Chen, C. L. H.; Shao, H. Subtyping of circulating exosome-bound amyloid β reflects brain plaque deposition. *Nat. Commun.* **2019**, *10*, 1144.
(46) Wang, Z.; Sun, X.; Natalia, A.; Tang, C. S. L.; Ang, C. B. T.; Ong, C. A. J.; Teo, M. C. C.; So, J. B. Y.; Shao, H. Dual-Selective Magnetic Analysis of Extracellular Vesicle Glycans. *Matter* **2020**, *2*, 150−166.
(47) Yang, L.; Huang, X.; Sun, L.; Xu, L. A piezoelectric immunosensor for the rapid detection of p16INK4a expression in liquid-based cervical cytology specimens. *Sens. Actuators, B* **2016**, *224*, 863−867.
(48) Duangkaew, P.; Tapaneeyakorn, S.; Apiwat, C.; Dharakul, T.; Laiwejpithay, S.; Kanatharana, P.; Laocharoensuk, R. Ultrasensitive electrochemical immunosensor based on dual signal amplification process for p16INK4a cervical cancer detection in clinical samples. *Biosens. Bioelectron.* **2015**, *74*, 673−679.
(49) Wang, X.; Wang, Y.; Shan, Y.; Jiang, M.; Gong, M.; Jin, X.; Wang, X.; Cheng, J. An electrochemiluminescence biosensor for detection of CdkN2A/p16 anti-oncogene based on functional electrospun nanofibers and core-shell luminescent composite nanoparticles. *Talanta* **2018**, *187*, 179−187.
(50) Sabate del Rio, J.; Henry, O. Y. F.; Jolly, P.; Ingber, D. E. An antifouling coating that enables affinity-based electrochemical biosensing in complex biological fluids. *Nat. Nanotechnol.* **2019**, *14*, 1143−1149.
(51) Studdert, D. M.; Hall, M. A. Disease Control, Civil Liberties, and Mass Testing — Calibrating Restrictions during the Covid-19 Pandemic. *N. Engl. J. Med.* **2020**, DOI: 10.1056/NEJMp2007637.

https://dx.doi.org/10.1021/acssensors.0c00599
ACS Sens. 2020, 5, 1864−1871